

Strain Engineering of Altermagnetic Symmetry in Epitaxial RuO₂ Films

Johnathas D. S. Forte,^{1,*} Seung Gyo Jeong,^{2,*} Anand Santhosh,²
Seungjun Lee,^{1,3,†} Bharat Jalan,^{2,‡} and Tony Low^{4,5,§}

¹*Department of Electrical and Computer Engineering,
University of Minnesota, Minneapolis, Minnesota 55455, USA*

²*Department of Chemical Engineering and Materials Science,
University of Minnesota-Twin Cities, Minneapolis, Minnesota 55455, USA*

³*Department of Applied Physics, Kyung Hee University, Yongin 17104, Republic of Korea*

⁴*Department of Electrical and Computer Engineering,
University of Minnesota, Minneapolis, Minnesota 55455 - USA*

⁵*School of Physics and Astronomy, University of Minnesota, Minneapolis, Minnesota 55455, USA*
(Dated: April 6, 2026)

The magnetic ground state of RuO₂ has been under intense debate. Using first-principles calculations, we show that compressive strain along [001] direction stabilizes an altermagnetic phase in RuO₂ thin films grown on (100) and (110) TiO₂ substrates. We further identify that compressive strain enhances the density of states near the Fermi level, resulting in a Fermi surface instability and the emergence of altermagnetism. The magnitude of strain and the associated increase in the density of states can be tuned by varying the film thickness, as systematically confirmed by x-ray diffraction and photoemission spectroscopy measurements. Symmetry analysis further reveals that (100) RuO₂ hosts an ideal altermagnetic order, whereas broken symmetry in (110) films leads to an uncompensated ferrimagnetic state. Finally, we discuss the effects of Hubbard U parameters and evaluate the realistic tunneling magnetoresistance of (100) RuO₂.

Introduction Altermagnetism, a recently identified collinear magnetic phase, exhibits compensated local magnetic moments while breaking time-reversal (\mathcal{T}) symmetry, leading to non-relativistic spin-momentum locking. [1–4] This unique property opens a novel possibility for energy-efficient and ultrafast spintronic applications, potentially overcoming the fundamental limitations of conventional ferromagnetic and antiferromagnetic spintronics. [5–7] After identifying the first altermagnetic material, RuO₂, [1, 8] significant research efforts have been dedicated to discovering novel altermagnetic materials. [9–15]

Despite these advancements, the magnetic ground state of RuO₂ still remains under intense debate. Early experimental studies using neutron diffraction [8] and resonant x-ray scattering [16] reported antiferromagnetic order in RuO₂, and density functional theory (DFT) calculations with the Hubbard U correction revealed its altermagnetic properties. [1, 2] These reports attracted explosive attention, and following experiments revealed signatures consistent with altermagnetic order. [17–23] However, more recently, conflicting evidence has emerged from x-ray diffraction (XRD), muon spin rotation and neutron diffraction experiments, which reported a non-magnetic ground state in bulk RuO₂ and/or in relatively thick films. [24–27] Subsequent experiment and theoretical results have also claimed its nonmagnetic ground state, further fueling the debate. [28–32]

It is notable that, when RuO₂ approaches the atomically thin limit, its altermagnetic behavior becomes more consistently observable, suggesting that both sample thickness and epitaxial strain play important roles in its magnetism. For instance, mirror-even spin splitting

have been observed in spin- and angle-resolved photoemission spectroscopy in a 2 nm (110) RuO₂ thin film. [33] Furthermore, second-harmonic generation measurements have revealed time-reversal symmetry breaking in ultrathin (<4 nm) (110) RuO₂ films epitaxially grown on (110) TiO₂, which is absent in bulk single crystal RuO₂, further underscoring the critical influence of epitaxial strain [34]. The observation of a sizable anomalous Hall effect in the ultrathin films consistently suggests a strain-driven stabilization of altermagnetic order [35]. Nevertheless, the fundamental physical relationship between altermagnetic order and the lattice parameters of RuO₂ remains largely unexplored.

Here, we systematically investigate the strain effects in RuO₂ films grown on TiO₂ substrates and their influence on magnetic order. The XRD measurements reveal that the lattice constants of RuO₂ strongly depend on film thickness due to epitaxial strain from the TiO₂ substrate. Our first-principles calculations show that compressive strain along the [001] direction enhances the density of states near the Fermi level, driving Fermi surface instabilities and stabilizing the altermagnetic phase. Notably, this strain-induced magnetism emerges in RuO₂ films on (100) and (110) oriented TiO₂ without requiring Hubbard U corrections or additional hole doping. Furthermore, we find that additional symmetry breaking in (110) RuO₂ induces an uncompensated ferrimagnetic order, in contrast to the ideal altermagnetic phase in (100) RuO₂. Finally, we analyze spin–momentum locking and the Fermi surface of altermagnetic (100) RuO₂, and evaluate the tunneling magnetoresistance ratio within a realistic range of Hubbard U parameters.

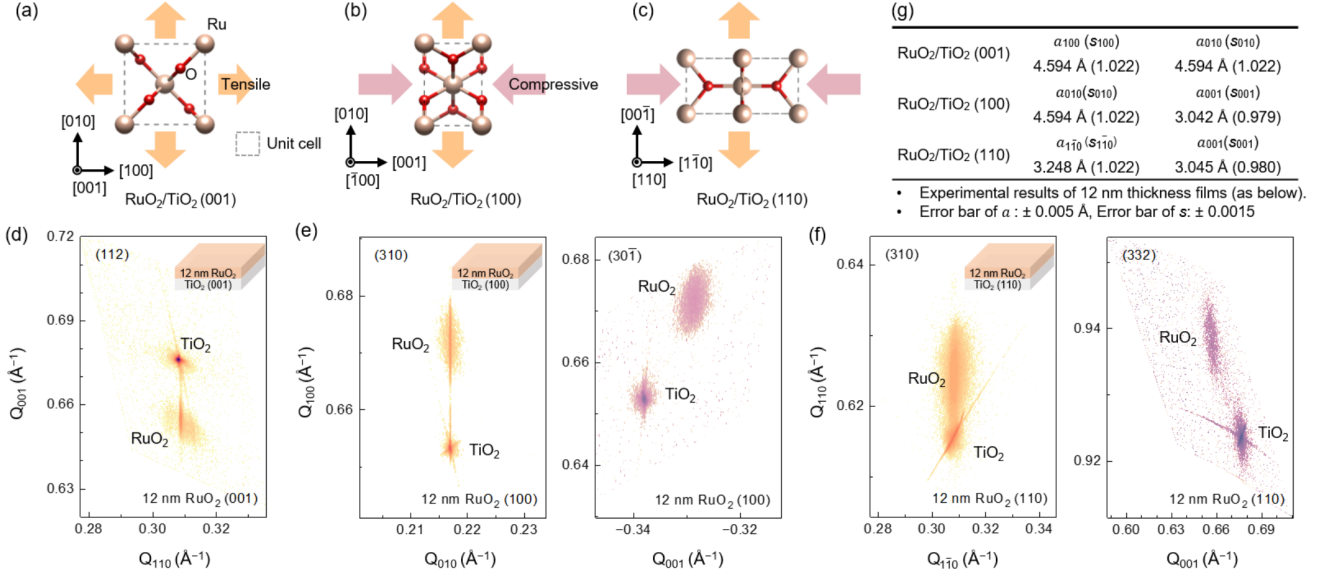


FIG. 1. (a-c) Schematic illustrations of epitaxial strain in RuO₂ films grown on TiO₂ substrates with three orientations: (001), (100), and (110). Orange and pink arrows represent tensile and compressive strain components, respectively. (d-f) XRD RSMs of 12 nm thick RuO₂ films grown on (001), (100), and (110) TiO₂ substrates. (g) Summary of lattice constants (with respect to the primitive unit cell) and calculated strain factors (s) for each crystallographic orientation of RuO₂/TiO₂ heterostructures.

Epitaxial strain of RuO₂ on TiO₂ substrate The lattice constants of RuO₂ thin films can be different from its bulk values. In the former, the substrate imposes epitaxial strain in RuO₂ arising from the lattice constant mismatch, which can vary depending on the crystallographic direction of epitaxial growth. At room temperature, bulk RuO₂ has tetragonal lattice constants of $a_{100}^{\text{RuO}_2} = a_{010}^{\text{RuO}_2} = 4.492$ Å and $a_{001}^{\text{RuO}_2} = 3.106$ Å, [36] while bulk TiO₂ has $a_{100}^{\text{TiO}_2} = a_{010}^{\text{TiO}_2} = 4.594$ Å and $a_{001}^{\text{TiO}_2} = 2.959$ Å. [37] Here, the subscripts represent the Miller indices for the crystallographic orientations.

For the (001) plane, as shown in Fig. 1(a), the in-plane lattice mismatch is isotropic; +2.2% along both [100] and [010] directions. For convenience, we define the epitaxial strain factor as $s_{hkl} = a_{hkl}^{\text{RuO}_2} / a_{hkl}^{\text{TiO}_2}$, where $a_{hkl}^{\text{RuO}_2}$ ($a_{hkl}^{\text{TiO}_2}$) is the lattice constant of strained (bulk) RuO₂ along the direction $[hkl]$, resulting in $s_{100} = s_{010} = 1.022$. In contrast, both (100) and (110) planes exhibit anisotropic lattice mismatch: -4.7% ($s_{001} = 0.953$) along [001] and +2.2% ($s_{010} = s_{1\bar{1}0} = 1.022$) along [100] or $[1\bar{1}0]$, shown in Fig. 1(b) and (c). To experimentally elucidate the strain state and its crystallographic anisotropy, we grew three different 12 nm RuO₂ films on TiO₂ (001), (100), and (110) substrates using hybrid molecular beam epitaxy (MBE). XRD reciprocal space mapping (RSM) was performed around asymmetric reflections for each sample, as shown in Fig. 1(d)-(f). For the (112) reflection of the 12 nm RuO₂/TiO₂ (001) film (Fig. 1(d)), the RuO₂ peak is vertically aligned with the TiO₂ substrate peak along the in-plane (110) reciprocal space vector (Q_{110}). This alignment indicates that the in-plane lattice con-

stants of RuO₂ are fully locked to those of the substrate, confirming coherent epitaxial strain. In contrast, for the RuO₂/TiO₂ (100) film (Fig. 1(e)), the (310) and (30-1) RSMs reveal anisotropic strain relaxation. While the RuO₂ peak remains vertically aligned with the substrate along Q_{010} , indicating coherent strain along that direction, the peak shifts laterally along Q_{001} . A similar anisotropic behavior is observed for the RuO₂/TiO₂ (110) film (Fig. 1(f)). The RuO₂ peak remains aligned with the substrate along $Q_{1\bar{1}0}$, whereas a clear lateral shift is observed along Q_{001} . This crystal direction-dependent relaxation along Q_{001} for both (100) and (110) cases evidence anisotropic in-plane lattice relaxation. The extracted lattice parameters and corresponding strain values are summarized in Fig. 1(g) and Table S1 in the Supplementary Information (SI)[38]. These experimentally quantified strain states provide a realistic structural basis for interpreting the theoretically predicted evolution of magnetic properties under anisotropic strain modulations.

Strain - magnetization phase diagrams To clearly understand the relation between the lattice parameter and magnetic ground state of RuO₂, we map the strain-magnetization phase diagram of (001), (100), and (110) RuO₂ through first-principles DFT calculations, as shown in Fig.2(a)-(c). The phase diagrams explore a range of strain states imposed by different types of substrates. Strain was simulated by varying the in-plane lattice constants for each case and finding the new equilibrium out-of-plane lattice constant. We highlight with red stars the points on the phase diagrams correspond-

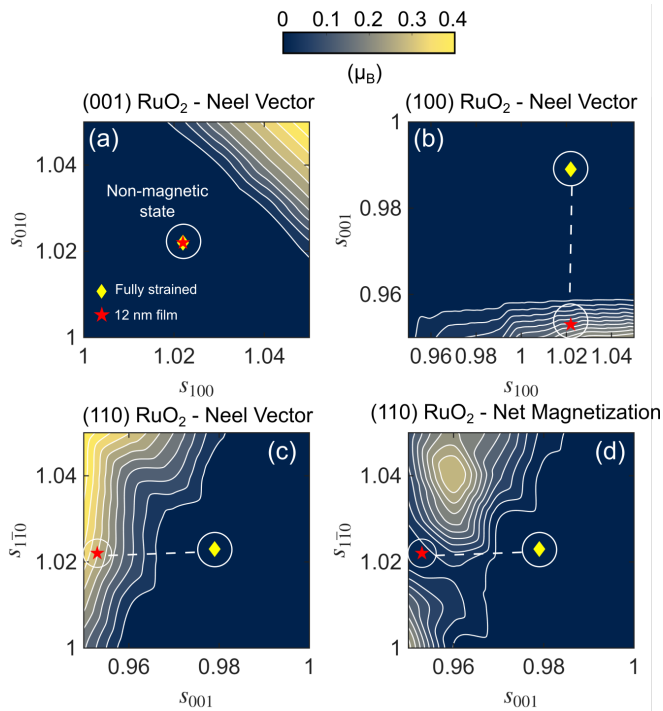


FIG. 2. Strain-magnetization Neel vector phase diagrams for (a) (001), (b) (100) and (c) (110) RuO₂. The red stars and yellow diamonds in each panel indicate lattice constants of fully strained and partially strained RuO₂ on TiO₂, respectively. (d) Strain-net magnetic moments for (110) RuO₂.

ing to fully strained RuO₂ films grown on TiO₂, estimated from the bulk lattice constants. By using XRD, although the fully strained lattice of a single RuO₂ film (< 4 nm) on TiO₂ (100) and (110) substrates could not be unambiguously resolved, fully strained ultrathin layers were observed in a 2 nm RuO₂/TiO₂ (110) superlattice [34]. In order to compare our theoretical calculations, we also add the yellow diamonds, which correspond to experimentally measured lattice constants of 12 nm films (i.e., partially strained). The magnetic properties in these phase diagrams are calculated entirely through *ab initio* methods, i.e., our experimental data refers to the lattice constants only. We note that these calculations were performed without including the Hubbard U correction, and the possible influence of this parameter will be discussed later. To quantitatively describe its altermagnetic properties, here, we defined the Néel vector magnitude as $N = |\vec{\mu}_{\text{Ru}_1} - \vec{\mu}_{\text{Ru}_2}|/2$ where $\vec{\mu}_{\text{Ru}_1}$ and $\vec{\mu}_{\text{Ru}_2}$ represent the two opposite local magnetic moments of the Ru atoms in the primitive cell. Additional details of the first-principles calculations are provided in the SI. [38]

For (001) RuO₂, we find that sufficiently large strains along the [100] and [010] axes can stabilize the altermagnetic phase, as shown in Fig. 2(a). However, the fully strained (001) RuO₂/TiO₂ film lattice constants lie within the nonmagnetic region of the phase diagram, in-

dicating the absence of magnetism in RuO₂ grown on (001) TiO₂. By contrast, as shown in Figs. 2(b) and (c), strong compressive strain along the [001] direction predominantly stabilizes finite magnetic moments in RuO₂, which can be realized in fully strained (100) and (110) films on TiO₂. These results are consistent with experimental observations of altermagnetic order in RuO₂ thin films, [34, 35] even without including any Hubbard U correction. Moreover, tensile strains along [100] and [1 $\bar{1}$ 0] directions, respectively, further enhance the magnetic moments. This secondary effect can be attributed to piezomagnetism in the rutile crystal structure. [39, 40] However, the Néel vector vanishes in 12 nm RuO₂ films due to strain relaxation along [001]. These results underscore the fragile nature of magnetism in RuO₂ thin films, [38] offering important design rules in stabilizing the magnetic ground state. Our XRD results indicate that, despite thickness-dependent changes in peak intensity and broadening, the lattice constants of strain-relaxed RuO₂ layers grown on (100) TiO₂ exhibit small variations between 7 and 13 nm, [38] consistent with previous reports using e-beam-assisted MBE. [41]

Beyond inducing local magnetism, epitaxial strain also alters the symmetry of the material. In particular, altermagnetism is characterized by proper or improper rotation, combined with time reversal that restores the original spin configuration. This symmetry is expressed by the spin-symmetry operation $[R_s||R_t]$, where the left (right) operator acts in spin (real) space. [2, 3, 7] For RuO₂, both $[C_2||C_{4z}\tau]$ and $[C_2||C_{2x}\tau]$ symmetries satisfy the altermagnetic condition, where C_2 denotes spin-space inversion, C_{4z} and C_{2x} are spatial rotations, and τ represents a half-translation. All these symmetries are preserved in fully strained (001) RuO₂, which remains in space group $P4_2/mnm$, as shown in Fig. 1(a). However, the absence of local magnetic moments in this geometry leads to a nonmagnetic ground state. In contrast, for (100) RuO₂, the $[C_2||C_{4z}\tau]$ symmetry is broken due to its orthorhombic lattice distortion. In this case, the space group is the orthorhombic $Pnmm$, which results in invariance under $[C_2||C_{2x}\tau]$. Together with the finite local magnetic moments arising from compressive strain, (100) RuO₂ yields the ideal altermagnetic phase, as shown in Fig. 1(b). In fully strained (110) RuO₂, both altermagnetic symmetries are completely broken, giving rise to a finite net magnetic moment. [35] To examine this, we explore the strain-net magnetic moment phase diagram of (110) RuO₂, defined as $m = |\vec{\mu}_{\text{Ru}_1} + \vec{\mu}_{\text{Ru}_2}|$, in Fig. 2(d). The net magnetization here is $\approx 0.025 \mu_B$. However, it becomes larger in regions with high anisotropy between a_{110} and $a_{1\bar{1}0}$. Thus, (110) RuO₂ is classified into a uncompensated ferrimagnet, which follows the same spin-space group configuration as a ferromagnet.

Origin of magnetism in RuO₂ Experimentally, altermagnetic signatures have also been reported in (001) and (101) RuO₂ thin films, indicating that the underlying

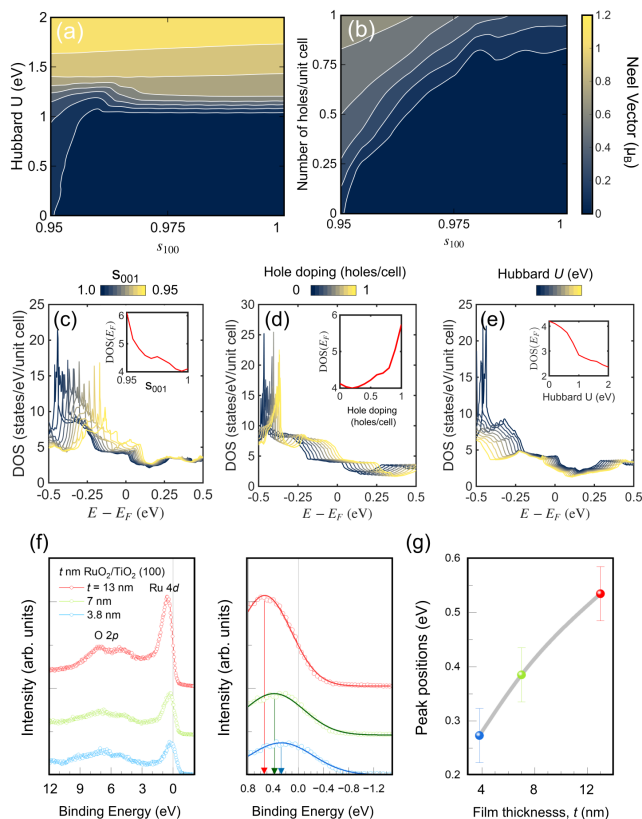


FIG. 3. (a) Hubbard U and (b) hole doping-strain phase diagrams for (100) RuO₂ showing the Neel vector. Density of states for (c) charge neutral (100) RuO₂ from pristine to fully strained, (d) unstrained (100) RuO₂ as a function of hole-doping and (e) unstrained, charge neutral (100) RuO₂ as a function of the Hubbard U strength. The insets show the increase of the density of states at the Fermi level, which dictates the itinerant electron magnetism in (c) and (d), while the decreasing DOS(E_F) in (e) reveals the localized character of this type of magnetism. (f) XPS valence band spectra of RuO₂ films on TiO₂ (100) substrates with different thickness t . The vertical arrows in the right panel indicate the estimated peak positions of the Ru 4d states, obtained by fitting with Voigt functions. (g) Summary of the Ru 4d peak positions as a function of t .

physics extends beyond simple strain effects. To clarify the microscopic origin of magnetism in RuO₂, we construct extended magnetic phase diagrams including hole doping and Hubbard U for (100) RuO₂, as shown in Fig. 3(a) and (b), respectively. We find that both hole doping [31] and finite U stabilize local magnetic order even without strain, thereby reducing the critical strain for the nonmagnetic–antiferromagnetic transition. For a given strain state, both Hubbard U and hole doping increase the local magnetic moment. Thus, both electron correlation and hole doping can contribute to promote magnetism at low strain in experiments. Consistently, we also observe hole-doping–induced magnetism in (110) RuO₂, further supporting the proposed mechanism. [38]

To further understand the physical origin of magnetism in RuO₂, we analyze the strain-, doping-, and U -dependent nonmagnetic density of states (DOS), shown in Fig. 3(c-e). For pristine RuO₂ with $U = 0$ eV, the DOS near the Fermi level (E_F) is relatively low, but a strong peak exists around $E = E_F - 0.45$ eV. Either compressive strain along [001] or hole doping shifts this peak toward E_F , thereby enhancing the DOS at E_F and triggering spontaneous magnetization via Stoner instability. [31, 35] In contrast, a finite U shifts the DOS in the opposite direction. This indicates that near $U \sim 0$ eV, itinerant magnetism arises from Fermi surface instability associated with high DOS, which is strain-sensitive, while larger U drives strain-independent localized magnetism.

At this point, it is important to discuss the reasonable magnitude of the Hubbard U for RuO₂. Recent experiments consistently suggest that $U > 1.2$ eV is highly unlikely. For example, the experimentally reported $|\vec{\mu}_{\text{Ru}}|$ of 0.05–0.15 μ_B is far below than the ~ 1.0 μ_B predicted by $U > 1.2$ eV. [8, 16] The absence of magnetism in high-purity bulk RuO₂ also supports a small U . [24, 25] Also, optical spectroscopy [30, 42] and spin-resolved ARPES [28, 33] further support $U \sim 0$. Therefore, the observed magnetism of RuO₂ in experiments is most likely understood as arising from strain- or doping-induced itinerant magnetism, with only a minor role for U -driven localization. Nonetheless, it is worth noting that a small but finite U is not fully excluded yet.

To validate the theoretically proposed strain scenario, we synthesized epitaxial RuO₂ films on TiO₂ (100) substrates with thicknesses of 3.8, 7, and 13 nm using hybrid molecular beam epitaxy (hMBE) (Figs. S1a–c and S2). [38] Structural characterizations by x-ray reflectometry (XRR) and XRD (Fig. S2) confirm high crystalline quality. XRD reciprocal space maps (RSMs) around the TiO₂ (30 $\bar{1}$) reflection reveal that the 3.8 nm film remains fully strained, while the 7 nm film shows a partially relaxed peak near $Q_{001} \approx -3.28 \text{ \AA}^{-1}$, which becomes more pronounced for the 13 nm film. [38] These results indicate a critical thickness for strain relaxation along [001] of ~ 4 nm, consistent with previous reports on RuO₂/TiO₂ (110) heterostructures [35, 42, 43]. The in-plane [010] lattice parameter remains coherently strained up to 13 nm (Table S1), suggesting that the strain effect primarily arises along the [001] direction.

Strain-dependent electronic structure modulation near the Fermi level was further examined using valence-band x-ray photoelectron spectroscopy (XPS) (Figs. 3(f)–(g), S4). [38] The spectra display O 2p states between 2 eV and 10 eV binding energy and Ru 4d states from 0 to 2 eV (Fig. 3(f), left) [44]. The right panel of Fig. 3(f) highlights the evolution of the Ru 4d feature near the Fermi level. The spectra were fitted with Voigt functions to extract peak positions, summarized in Fig. 3(g). The Ru 4d peak systematically shifts toward the Fermi level as the film thickness decreases from 13 nm to 3.8 nm.

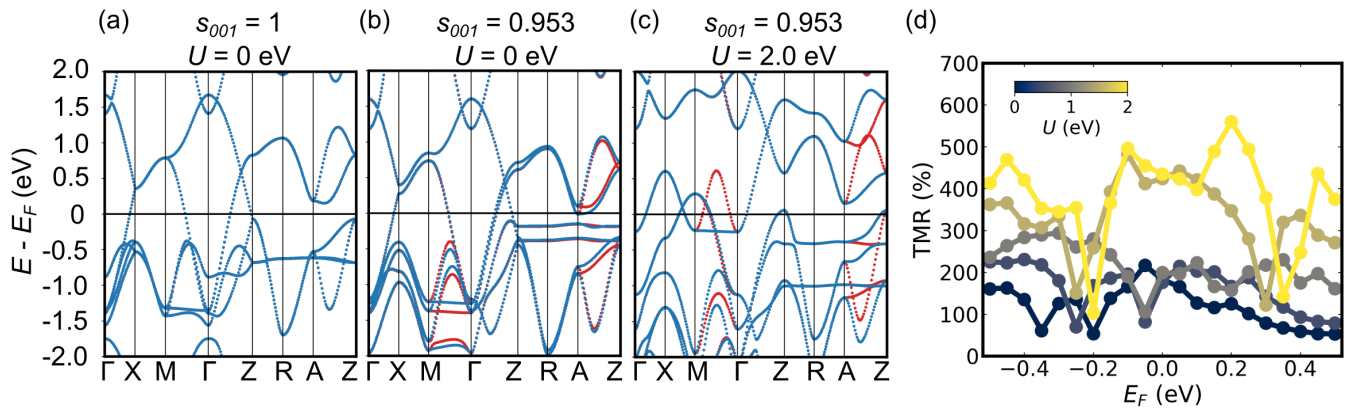


FIG. 4. Band structures for (a) unstrained (100) RuO₂ with $U = 0$ eV and fully strained (100) RuO₂ with (b) $U = 0$ eV and (c) $U = 2$ eV. Strain alone can drive the spin-splitting of the bands, which is further enhanced by the Hubbard U interaction. In (d), we evaluate the TMR as a function of the Fermi level for different U , showing that it increases for larger spin-splittings, as expected.

This observation demonstrates that epitaxial strain along [001] drives the Ru 4d valence state closer to the Fermi level [42], in agreement with our theoretical calculations.

Re-evaluation of electronic structure of (100) RuO₂
To re-evaluate the electronic structure of RuO₂, we compared the band structures of pristine, strained, and combined strained with Hubbard U RuO₂, as shown in Fig. 4(a-c). Without U , the band structure of alternating (strained) RuO₂ closely resembles that of the nonmagnetic (pristine) phase. Under compressive strain, the flat band along Z-R-A-Z shifts toward E_F , thereby enhancing the density of states. The spin splitting energy in (100) RuO₂ is on the order of several tens of meV, which is much smaller than the 1.4 eV predicted for $U = 2$ eV, [2] mainly along the M- Γ line.

Finally, we evaluate tunneling magnetoresistance (TMR) of magnetic tunnel junction (MTJ) based on (100) RuO₂. To estimate the TMR, we developed a simple model based on Julliere's approach, [45] defined as $\text{TMR} \equiv (R_{ap} - R_p)/R_p$, where R_p and R_{ap} are the resistances in parallel and anti-parallel state configurations, respectively. The resistances are in turn estimated through the overlap of the Fermi surfaces, calculated using the spin-dependent spectral function $A_\sigma(\mathbf{k}, \omega) = \frac{1}{\pi} \text{Im}(\hbar\omega - \epsilon_{\mathbf{k},\sigma} - i\eta)^{-1}$ as follows

$$K_{\sigma\sigma'}(\omega) = \frac{\int_{BZ} d^3k A_\sigma(\mathbf{k}, \omega) A_{\sigma'}(\mathbf{k}, \omega)}{\int_{BZ} d^3k [|A_\uparrow(\mathbf{k}, \omega)|^2 + |A_\downarrow(\mathbf{k}, \omega)|^2]}, \quad (1)$$

where $\sigma = \uparrow, \downarrow$ is the spin index and the broadening factor of η is chosen to be 1 meV. Then, we simply assume that the resistances are proportional to the inverse of the overlap $K_{\sigma\sigma'}(\omega)$, $R_p = 1/K_{\uparrow\uparrow}$ and $R_{ap} = 1/K_{\uparrow\downarrow}$. We emphasize that this model ignores the microscopic structure of the insulating barrier. [45]

Our results are summarized in Fig. 4(d). For $U < 1.2$ eV, the TMR at E_F is nearly insensitive to U and remains at a maximum of approximately 200%. With larger U , strong spin splitting along M- Γ at E_F emerges, enhancing the TMR up to $\sim 600\%$. However, as discussed earlier, such strong U values are likely unrealistic and may lead to an overestimation of TMR. Nevertheless, the TMR can be further improved by selecting an appropriate insulating barrier that minimizes R_p through optimizing momentum-dependent spin-polarized conduction. [46, 47] The detailed spin-resolved Fermi surface of (100) RuO₂ is provided in Supplementary Information. [38] We further note that a nonzero TMR is also expected in (110) RuO₂, but not in (001) RuO₂ due to the absence of local magnetism.

Conclusion In summary, combining XRD measurements with first-principles calculations, we demonstrate that epitaxial strain plays a crucial role in RuO₂ thin films by manipulating their magnetic ground state. Compressive strain along [001] enhances the density of states near E_F , driving Fermi surface instabilities and itinerant altermagnetism. Experimentally, (100) and (110) RuO₂ films grown on TiO₂ substrates satisfy these conditions, with the former exhibiting ideal altermagnetism and the latter showing ferrimagnetism due to broken rotation symmetries. We re-evaluate its spin-splitting energy and corresponding TMR of a (100) RuO₂-based MTJ structure, both of which are found to be smaller than previously reported values. Our results provide a fundamental understanding of the origin of altermagnetism in RuO₂ and thus reconcile the ongoing debate surrounding its magnetic nature.

Acknowledgements This work was supported by AFOSR sponsored MURI (Grant #FA9550-25-1-0262).

* These authors contributed equally to this work.

† sjunlee@khu.ac.kr

‡ bjalan@umn.edu

§ tlow@umn.edu

- [1] L. Šmejkal, R. González-Hernández, T. Jungwirth, and J. Sinova, *Sci. Adv.* **6**, eaaz8809 (2020).
- [2] L. Šmejkal, J. Sinova, and T. Jungwirth, *Phys. Rev. X* **12**, 040501 (2022).
- [3] L. Šmejkal, J. Sinova, and T. Jungwirth, *Phys. Rev. X* **12**, 031042 (2022).
- [4] L.-D. Yuan, Z. Wang, J.-W. Luo, and A. Zunger, *Phys. Rev. Mater.* **5**, 014409 (2021).
- [5] D.-F. Shao, S.-H. Zhang, M. Li, C.-B. Eom, and E. Y. Tsymlal, *Nat. Commun.* **12**, 7061 (2021).
- [6] L. Šmejkal, A. Marmodoro, K.-H. Ahn, R. González-Hernández, I. Turek, S. Mankovsky, H. Ebert, S. W. D'Souza, O. Šipr, J. Sinova, *et al.*, *Phys. Rev. Lett.* **131**, 256703 (2023).
- [7] L. Bai, W. Feng, S. Liu, L. Šmejkal, Y. Mokrousov, and Y. Yao, *Adv. Funct. Mater.* **34**, 2409327 (2024).
- [8] T. Berlijn, P. C. Snijders, O. Delaire, H.-D. Zhou, T. A. Maier, H.-B. Cao, S.-X. Chi, M. Matsuda, Y. Wang, M. R. Koehler, *et al.*, *Phys. Rev. Lett.* **118**, 077201 (2017).
- [9] J. Krempaský, L. Šmejkal, S. D'souza, M. Hajlaoui, G. Springholz, K. Uhlřřová, F. Alarab, P. Constantinou, V. Strocov, D. Usanov, *et al.*, *Nature* **626**, 517 (2024).
- [10] S. Lee, S. Lee, S. Jung, J. Jung, D. Kim, Y. Lee, B. Seok, J. Kim, B. G. Park, L. Šmejkal, *et al.*, *Phys. Rev. Lett.* **132**, 036702 (2024).
- [11] Z. Zhou, X. Cheng, M. Hu, R. Chu, H. Bai, L. Han, J. Liu, F. Pan, and C. Song, *Nature*, 1 (2025).
- [12] L. Han, X. Fu, R. Peng, X. Cheng, J. Dai, L. Liu, Y. Li, Y. Zhang, W. Zhu, H. Bai, *et al.*, *Sci. Adv.* **10**, eadn0479 (2024).
- [13] R. Takagi, R. Hirakida, Y. Settai, R. Oiwa, H. Takagi, A. Kitaori, K. Yamauchi, H. Inoue, J.-i. Yamaura, D. Nishio-Hamane, *et al.*, *Nat. Mater.* **24**, 63 (2025).
- [14] B. Jiang, M. Hu, J. Bai, Z. Song, C. Mu, G. Qu, W. Li, W. Zhu, H. Pi, Z. Wei, Y.-J. Sun, Y. Huang, X. Zheng, Y. Peng, L. He, S. Li, J. Luo, Z. Li, G. Chen, H. Li, H. Weng, and T. Qian, *Nat. Phys.* **21**, 754 (2025).
- [15] F. Zhang, X. Cheng, Z. Yin, C. Liu, L. Deng, Y. Qiao, Z. Shi, S. Zhang, J. Lin, Z. Liu, M. Ye, Y. Huang, X. Meng, C. Zhang, T. Okuda, K. Shimada, S. Cui, Y. Zhao, G.-H. Cao, S. Qiao, J. Liu, and C. Chen, *Nat. Phys.* **21**, 760 (2025).
- [16] Z. Zhu, J. Strempler, R. Rao, C. Occhialini, J. Pellicciari, Y. Choi, T. Kawaguchi, H. You, J. Mitchell, Y. Shao-Horn, *et al.*, *Phys. Rev. Lett.* **122**, 017202 (2019).
- [17] Z. Feng, X. Zhou, L. Šmejkal, L. Wu, Z. Zhu, H. Guo, R. González-Hernández, X. Wang, H. Yan, P. Qin, *et al.*, *Nat. Electron.* **5**, 735 (2022).
- [18] T. Tschirner, P. Keßler, R. D. Gonzalez Betancourt, T. Kotte, D. Kriegner, B. Büchner, J. Dufouleur, M. Kamp, V. Jovic, L. Smejkal, *et al.*, *APL Mater.* **11** (2023).
- [19] A. Bose, N. J. Schreiber, R. Jain, D.-F. Shao, H. P. Nair, J. Sun, X. S. Zhang, D. A. Muller, E. Y. Tsymlal, D. G. Schlom, *et al.*, *Nat. Electron.* **5**, 267 (2022).
- [20] H. Bai, L. Han, X. Feng, Y. Zhou, R. Su, Q. Wang, L. Liao, W. Zhu, X. Chen, F. Pan, *et al.*, *Phys. Rev. Lett.* **128**, 197202 (2022).
- [21] C.-T. Liao, Y.-C. Wang, Y.-C. Tien, S.-Y. Huang, and D. Qu, *Phys. Rev. Lett.* **133**, 056701 (2024).
- [22] M. Weber, S. Wust, L. Haag, A. Akashdeep, K. Leckron, C. Schmitt, R. Ramos, T. Kikkawa, E. Saitoh, M. Kläui, *et al.*, arXiv preprint arXiv:2408.05187 (2024).
- [23] O. Fedchenko, J. Minár, A. Akashdeep, S. W. D'Souza, D. Vasilyev, O. Tkach, L. Odenbreit, Q. Nguyen, D. Kutnyakhov, N. Wind, *et al.*, *Sci. Adv.* **10**, eadj4883 (2024).
- [24] M. Hiraiishi, H. Okabe, A. Koda, R. Kadono, T. Muroi, D. Hirai, and Z. Hiroi, *Phys. Rev. Lett.* **132**, 166702 (2024).
- [25] P. Keßler, L. Garcia-Gassull, A. Suter, T. Prokscha, Z. Salman, D. Khalyavin, P. Manuel, F. Orlandi, I. I. Mazin, R. Valentí, *et al.*, npj Spintronics **2**, 50 (2024).
- [26] C. A. Occhialini, C. Nelson, A. Bombardi, S. Fan, R. Acevedo-Esteves, R. Comin, D. N. Basov, M. Musashi, M. Kawasaki, M. Uchida, *et al.*, arXiv preprint arXiv:2510.13767 (2025).
- [27] L. Kiefer, F. Wirth, A. Bertin, P. Becker, L. Bohatý, K. Schmalzl, A. Stunault, J. A. Rodríguez-Velamazán, O. Fabelo, and M. Braden, *J. Phys. Condens. Matter* **37**, 135801 (2025).
- [28] J. Liu, J. Zhan, T. Li, J. Liu, S. Cheng, Y. Shi, L. Deng, M. Zhang, C. Li, J. Ding, *et al.*, *Phys. Rev. Lett.* **133**, 176401 (2024).
- [29] X. Peng, Z. Liu, S. Zhang, Y. Zhou, Y. Sun, Y. Su, C. Wu, T. Zhou, L. Liu, Y. Li, *et al.*, *Commun. Mater.* **6**, 177 (2025).
- [30] M. Wenzel, E. Uykur, S. Rößler, M. Schmidt, O. Janson, A. Tiwari, M. Dressel, and A. A. Tsirlin, *Phys. Rev. B* **111**, L041115 (2025).
- [31] A. Smolyanyuk, I. I. Mazin, L. Garcia-Gassull, and R. Valentí, *Phys. Rev. B* **109**, 134424 (2024).
- [32] D. Wickramaratne, M. Currie, S. S. Fields, C. D. Cress, and S. P. Bennett, arXiv preprint arXiv:2502.08872 (2025).
- [33] Y. Zhang, S. G. Jeong, L. Buiarelli, S. Lee, Y. Guo, J. Wen, H. Li, S. Nair, I. H. Choi, Z. Ren, Z. Yue, A. Fedorov, S.-K. Mo, J. Kono, J. S. Lee, T. Low, T. Birol, R. M. Fernandes, M. Radovic, B. Jalan, and M. Yi, arXiv preprint arXiv:2509.16361 (2025).
- [34] S. G. Jeong, I. H. Choi, S. Nair, L. Buiarelli, B. Pourbahari, J. Y. Oh, B. Y. Lin, J. M. LeBeau, N. Bassim, D. Hirai, *et al.*, *Proc. Natl. Acad. Sci.* **123**, e2526641123 (2026).
- [35] S. G. Jeong, S. Lee, B. Lin, Z. Yang, I. H. Choi, J. Y. Oh, S. Song, S. w. Lee, S. Nair, R. Choudhary, *et al.*, *Proc. Natl. Acad. Sci.* **122**, e2500831122 (2025).
- [36] T. Berlijn, P. C. Snijders, O. Delaire, H.-D. Zhou, T. A. Maier, H.-B. Cao, S.-X. Chi, M. Matsuda, Y. Wang, M. R. Koehler, P. R. C. Kent, and H. H. Weitering, *Phys. Rev. Lett.* **118**, 077201 (2017).
- [37] J. K. Burdett, T. Hughbanks, G. J. Miller, J. W. J. Richardson, and J. V. Smith, *J. Am. Chem. Soc.* **109**, 3639 (1987).
- [38] See Supplemental Material at URL-will-be-inserted-by-publisher for more details on the experiment and other theoretical results.
- [39] T. Moriya, *J. Phys. Chem. Solids.* **11**, 73 (1959).
- [40] M. Komuro, T. Aoyama, and K. Ohgushi, *Phys. Rev. B* **111**, 214445 (2025).

- [41] N. Wadehra, B. Z. Gregory, S. Zhang, N. Schnitzer, Y. Iguchi, Y. Evan Li, B. Pamuk, D. A. Muller, A. Singer, K. M. Shen, and D. G. Schlom, *Commun. Mater.* **6** (2025).
- [42] S. G. Jeong, I. H. Choi, S. Lee, J. Y. Oh, S. Nair, J. H. Lee, C. Kim, A. Seo, W. S. Choi, T. Low, *et al.*, *Sci. Adv.* **11**, eadw7125 (2025).
- [43] S. G. Jeong, B. Y. Lin, M. Jin, I. H. Choi, S. Lee, Z. Yang, S. Nair, R. Choudhary, J. Parikh, A. Santhosh, *et al.*, *Nat. Commun.* (2026).
- [44] V. Stoeberl, E. B. Guedes, F. Abud, R. F. Jardim, M. Abbate, and R. J. O. Mossaneck, *Europhys. Lett.* **132**, 47004 (2020).
- [45] M. Julliere, *Phys. Lett. A* **54**, 225 (1975).
- [46] Y.-Y. Jiang, Z.-A. Wang, K. Samanta, S.-H. Zhang, R.-C. Xiao, W. Lu, Y. Sun, E. Y. Tsymbal, and D.-F. Shao, *Phys. Rev. B* **108**, 174439 (2023).
- [47] G. Gurung, M. Elekhtiar, Q.-Q. Luo, D.-F. Shao, and E. Y. Tsymbal, *Nat. Commun.* **15**, 10242 (2024).